Mechanisms of dilatancy in rock salt at the grain-scale and implications for the dilatancy boundary

B.G.A. van Oosterhout[1], S.J.T. Hangx[1], C.J. Spiers[1]*

[1]HPT laboratory, Department of Earth Sciences, Utrecht University, The Netherlands

** b.g.a.vanoosterhout@uu.nl*

ABSTRACT: This paper presents an experimental investigation of the dilatancy boundary in rock salt based on triaxial compression tests (room temperature $10^{-5}s^{-1}$) of naturally wet and dried Leinesteinsalz samples. The experiments indicate that dilatancy in the Leinesteinsalz is observed at confining pressures $\leq 15\,MPa$, while at higher confining pressure mechanical behavior is non-dilatant. Two microphysical models were constructed based on mechanisms based on (1) intergranular slip and tensile failure and (2) the opening of voids due to plastic strain misfits between individual grains. A comparison of the experimental data with the first model indicates that slip on grain boundaries can only occur when the friction on the grain boundaries is lowered by the presence of fluid inclusions. The absence of any significant difference between dilatancy in dry and wet Leinesteinsalz eliminates the possibility that dilatancy is controlled by intergranular slip. The second model shows the typical type of behavior observed in the experiment with initial compaction and a later switch to dilatancy as axial strain progresses but fails to show a switch to compaction-only behavior at high confinement. Hence, dilatancy in rock salt is likely to be controlled by the opening of voids related to misfit strains, but the model needs to be modified.

1 Introduction

Natural rock salt formations are characterized by extremely low permeability, high ductility and high sealing capacity, making salt an excellent host rock for geological storage and disposal facilities. Nonetheless, the creation of underground cavities and excavations in rock salt disturbs the original stress state of the rock salt, resulting in an increase in deviatoric stress and a decrease in mean stress around the cavity walls (Tsang et al. 2005). Under these conditions, dense rock salt dilates via microcracking, leading to a positive volume change and an increase in porosity and permeability (Peach et al. 2001). The extent of dilatancy in this excavation disturbed or damage zone (EDZ), as well as the impact of dilatancy on the transport properties, are of key importance for assessing the safety of radioactive waste storage and disposal facilities in salt (Alkan et al. 2007). Recently, the extent of the EDZ has also gained attention in relation to a) the integrity of solution-mined storage caverns for renewably derived hydrogen or compressed air (Khaledi et al. 2016), and b) the long-term fate of abandoned, brine-filled caverns (Bérest & Brouard 2003). It is also of interest in the context of the self-sealing potential of abandoned hydrocarbon wellbores in rock salt caprocks (Orlic & Buijze 2014; Buijze et al. this volume).

The stress conditions at which dilatancy occurs have been measured experimentally and are typically determined based on sample-scale measurements of volumetric strain and permeability (Peach 1991) and/or acoustic phenomena (Popp et al. 2001), made during triaxial tests. In most of these experiments, the onset of dilatancy, or the “dilatancy boundary”, is defined as the minimum in the volumetric strain versus axial strain curve (dilatancy defined as positive). The empirically derived relationship indicates that the dilatancy boundary can be represented in differential or equivalent stress (σ_{eq}) vs. mean stress space ($\bar{\sigma}$). However, to date, no microphysical basis for the dilatancy boundary has been proposed that would provide a basis for extrapolation beyond lab conditions and time scales, or to more complex deformation paths.

The present study reports triaxial experiments on Leinesteinsalz samples carried out over a broad range of confining pressure ($2.5 - 40\ MPa$) on both naturally wet rock salt (i.e. with natural brine content) and on artificially dried rock salt. In addition, for the "wet" experiments, permeametry measurements were performed before and after the triaxial experiments. The aim is to test preliminary microphysical models for dilatancy development in deforming rock salt, based on the physical and/or chemical processes playing a role at the grain-scale. Two models are presented here. One is based on microcracks forming as a result of slip on inclined grain boundaries, causing tensile cracks to open on boundaries subparallel to the compression direction. A second model is based on the opening of voids due to plastic misfit strains between individual grains, related to a lack of five easy slip systems.

2 Experimental method

The present approach involved conventional triaxial deformation tests in combination with permeametry was performed on natural Leinesteinsalz samples (Zechstein Z2), at room temperature and relatively rapid strain rates ($4.8 \cdot 10^{-5}\ s^{-1}$). The deformation experiments were performed using the dilatometric triaxial apparatus (designed by H.C. Heard, described in detail by Peach 1991) at systematically varied confining pressures (P_c) ranging from 5 to 22.5 MPa. Confining pressure intervals of 2.5 MPa were explored to locate the transition from non-dilatant to dilatant behavior within that resolution. A first set of experiments was performed with no special sample pre-treatment, (i.e. on samples containing their inherent water content reached under storage conditions). In these runs, a saturated brine pressure of 2.5 MPa was applied to the sample ends and brine permeability measurements were made before and after the deformation experiment. After preparing and sealing the samples, the assembly was placed into the main pressure vessel and the pore fluid system was filled with 100% saturated brine. To close any pre-existing cracks that may have been formed during coring and machining, the confining pressure was first brought up to 25 MPa and maintained for 60 minutes, before lowering to the desired experimental value. The fluid permeability was measured before and after removal of the differential stress in each deformation experiment using transient step permeametry, which entails the measurement of the pressure decay due to flow-through following the application of a fluid pressure difference across the sample ends. This method has been widely described and used successfully for low porosity and low permeability rocks, using gases and liquids (see Peach 1991; Sutherland & Cave 1980; Trimmer 1982). A second set of experiments (two tests) was performed in an identical manner but on samples that were pre-treated and dried under vacuum for a period of two months at $50℃$, without applying brine pressure and without making permeability measurements.

3 Results

The experiments performed to investigate dilatancy in the Leinesteinsalz samples are listed in Table 1, along with the experimental conditions and data on the initial and final state of the samples. The two tests performed to investigate the effect of drying the samples on the dilatancy boundary are listed in the second block of Table 1.

At low confining pressures ($< 10\ MPa$), the volumetric strain curves indicate compaction in the early stages of loading, while at a few percent axial strain ($0 - 3\%$) a clear turn-around point is observed, marking the switch to dilatant behavior. At intermediate confining pressures ($12.5\ MPa - 15\ MPa$), such a turn-around point can still be identified, but the amount of positive volume change after this minimum point is minor (see Table 1). At confining pressures above $15\ MPa$, no turn-around point can be identified, and the mechanical behavior is non-dilatant throughout the entire experiment. The stress-strain curves in all experiments are non-linear from the onset of loading, indicating work hardening plastic flow. The axial strain, volumetric strain and differential stress of this turn-around point are shown in Table 1. Hence, a clear progression from dilatant behavior up to $P_c = 10 - 12.5\ MPa$ to non-dilatant behavior at P_c of

$15\ MPa$ and higher. No significant difference between wet and dry dilatancy experiments at the same mean effective stress was observed. This implies that the mechanical behavior of a wet experiments with an applied brine pressure of 2.5 MPa is similar to a dry experiment (without applied brine pressure) at 2.5 MPa lower confining pressure.

Table 1: List of deformation experiments on Leinesteinsalz shortened at strain rates of $4.8 \cdot 10^{-5}\ s^{-1}$. σ_{dil}, ε_{ax_dil} and ε_{v_dil} represent the differential stress, axial strain and volumetric strain at the point where dilatancy occurs, ε_{ax_tot} and ε_{v_tot} represent the axial and volumetric strain at the end of the experiment. $\kappa_{initial}$ and κ_{final} represent the permeability, measured within the machine at the imposed confining pressure, before and after the experiment.

Specimen number		P_c (MPa)	P_p (MPa)	σ_{dil} (MPa)	ε_{ax_dil} (%)	ε_{v_dil} (%)	$\varepsilon_{ax\ tot}$ (%)	$\varepsilon_{v\ tot}$ (%)	$\kappa_{initial}$ (m²)	κ_{final}(m²)
356/016 TC	Wet	5.0	2.5	13.30	0.36	-0.01	10.04	+2.18	$<10^{-21}$	$3.92 \cdot 10^{-16}$
356/028 TC	Wet	7.5	2.5	25.24	2.40	-0.31	11.62	+0.29	x	x
356/030 TC	Wet	10.0	2.5	26.47	2.83	-0.10*	11.17	+0.03*	$<10^{-21}$	$1.96 \cdot 10^{-18}$
356/024 TC	Wet	12.5	2.5	43.34	7.15	-0.34	12.01	-0.35	$2.07 \cdot 10^{-20}$	$6.54 \cdot 10^{-19}$
356/036 TC	Wet	15.0	2.5	44.61	5.73	-0.21	11.14	-0.24	$1.52 \cdot 10^{-20}$	$2.03 \cdot 10^{-19}$
356/040 TC	Wet	22.5	2.5	n/a	n/a	n/a	12.50	-0.41	$<10^{-21}$	$3.62 \cdot 10^{-20}$
356/037 TC	Wet	40.0	2.5	n/a	n/a	n/a	16.12	-0.53	$<10^{-21}$	$<10^{-21}$
356/033 TC	Dry	2.5	0	7.94	0.21	-0.01	10.48	+1.76	x	x
356/035 TC	Dry	7.5	0	34.38	3.16	-0.16	11.61	+0.27	x	x

* determined from pore volume change
X not measured
n/a not available: no minimum/turn-around point is reached during the experiment

The initial permeability of most samples subjected to permeametry are below the measurable resolution and hence smaller than $10^{-21}\ m^2$. However, for samples 356/024 TC and 356/036 TC a permeability of respectively $2.07 \cdot 10^{-20}\ m^2$ and $1.52 \cdot 10^{-20}\ m^2$ was determined (see Table 1). At all confining pressures, except at $40\ MPa$, an increase in permeability was observed after deformation. At $5\ MPa$, the permeability increased by five orders of magnitude; at $10\ MPa$, the increase was three orders of magnitude. At $40.0\ MPa$, the permeability remained below 10^{-21} m² (i.e. below the resolution limit) as in the undeformed state.

Based on the experimental results, the switch from non-dilatant to dilatant behavior for Leinesteinsalz can be presented in terms of differential stress vs. increasing confining pressure. Most experiments on dilatancy are performed without applying a pore pressure (e.g. Peach & Spiers 1996; Popp & Kern 2001) and in those experiments the mean effective stress is equal to the mean stress. In order to compare the experimental data in this study with other experimental data on dilatancy, the dilatancy boundary here is shown as a function of mean effective stress ($\left[\frac{\sigma_1+2\sigma_3}{3}\right] - P_f$).

A switch to dilatancy is observed at experiments below $15.0\ MPa$. At $22.5\ MPa$ and $40.0\ MPa$ no minimum is reached in the external volume change and the change in the internal volume is considered insignificant to define a minimum at $22.5\ MPa$ and absent at $40.0\ MPa$ as well. Therefore, the dilatancy boundary is defined based on the volumetric strain data up to $15.0\ MPa$ confining pressure. Based on the experimental data from this study on Leinesteinsalz, we suggest that the data is described most accurately by a linear dilatancy boundary, given by $\sigma_{eq} = 1.56\bar{\sigma} + 3.47$ (see Figure 1a). Samples 356/033 TC and 356/035 TC were pre-treated and dried under vacuum for a period of two months at 50℃, before

deformation at respectively $2.5\ MPa$ and $7.5\ MPa$. The stress conditions at the absolute minimum in the volumetric strain curve for dry and wet Leinesteinsalz are shown in Figure 1b. Note that for the wet experiments, the assumption is made that pore fluid penetrates the sample pore space. Therefore, the stress evolution paths of the wet experiments at $5.0\ MPa$ and $10.0\ MPa$ coincide with the dry experiments at respectively $2.5\ MPa$ and $7.5\ MPa$.

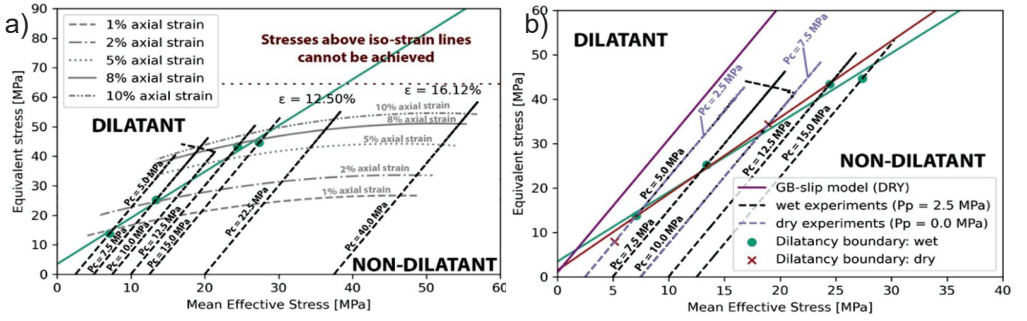

Figure 1: (a) Dilatancy boundary as a function of mean effective stress and Von Mises equivalent stress (differential stress) in "wet" Leinesteinsalz. The stress evolution of the individual experiments, shown in black and the grey envelopes, show the stress supported at different axial strains. (b) Dilatancy boundary in "wet" (green line) vs dry (brown line) Leinesteinsalz. As a reference, the theoretical prediction by the GBFS model for dry rock salt is shown.

Note that in this study, the "wet" experiments are all performed with a pore pressure of $2.5\ MPa$, theoretically lowering the mean effective stress by an equal amount. This relies on the assumption that the pore fluid can penetrate the pore space, requiring interconnection of these pores and is only valid once the rock salt has become dilatant. However, the fluid pressure can force the transfer of intrusion to the cracks and thus serving as an internal drive for the opening and growth of cracks and promote dilatancy (Alkan et al. 2007). Therefore, prior to the dilatancy boundary the pore pressure may already have some effect. Also note that when including the progression of axial strain for all "wet" experiments, it can be observed that the dilatancy boundary crosses the $1-2\%$ axial strain line for the experiment at $5-7.5\ MPa$ confinement and $5-8\%$ strain for $10-12.5\ MPa$ confinement. It is evident that at higher confining pressures the conditions required for dilatancy are not reached in these experiments. Additional strain beyond 10% hardly results in any further increase in differential stress on the rock salt and hence the differential stresses required for dilatancy occur at high confining pressures are not feasible. This is substantiated by the absence of a permeability increase after deformation in rock salt deformed at $40\ MPa$.

4 Models describing dilatancy in rock salt

While a lot of research has been aimed at quantifying dilatancy and the dilatancy boundary for various types of rock salt, at a range of confining pressures and for different deformation rates, relatively little effort has been made to explain why dilatancy occurs at the conditions observed in experiments. Peach & Spiers 1996 and Alkan 2009 have derived models to explain the observed increase in permeability in relation to dilatancy and microcrack linkage, using percolation theory. However, these do not explain under which conditions dilatancy in rock salt occurs, beyond empirical and/or phenomenological model fits. A preliminary attempt is made here to explore microphysical models that can mechanistically account for the onset of dilatancy in deforming rock salt, based on the physical and chemical processes operating at the grain scale.

4.1 Grain boundary frictional slip (GBFS) model

Peach 1991 and Hunsche 1998 have concluded that the dilatancy boundary is only dependent on deviatoric and mean stress and does not significantly vary between different salt types. They and other authors (e.g. Alkan et al. 2009; Popp et al. 2001) accordingly treat the dilatancy boundary as resembling a yield or failure criterion. At differential stresses above this boundary, microcracks are generated, creating excess lateral strains (volumetric strain) and resulting in a rapid increase in permeability. Microstructural evidence suggests that microcracks are generated on grain boundaries that are orientated parallel to σ_1 (Peach 1991, Peach & Spiers 1996). This suggests shear failure or slip on grain boundaries orientated at a favorable angle to σ_1, in combination with tensile opening of grain boundaries orientated subparallel to σ_1, may be responsible for generating dilatant microcracking in rock salt during plastic deformation. In the following, a model is developed to assess this possibility.

As starting point, consider an idealized 2-D rock salt microstructure consisting of hexagonal grains, defined by the apical angle (ψ) and aspect ratio (height/width) ($R = \frac{h}{w}$) (see Figure 2). Given that experiments on dilatancy in general are performed under axi-symmetric conditions ($\sigma_2 = \sigma_3$), we assume that the onset of dilatancy can be treated as a 2D problem (c.f. Coulomb failure). On type A grain boundaries (Figure 2), sliding is expected once the shear stress ($\tilde{\tau}_A$) exceeds a critical grain boundary shear strength and when the normal tensile stress on type D grain boundaries ($\tilde{\sigma}_D$) exceeds the tensile strength ($\tilde{T}_0$). The criterion for shear failure is assumed to be expressible by a coulomb frictional slip criterion expressed by: $\tilde{\tau}_A = \tilde{\mu}\,\tilde{\sigma}_A + S_0$, in which $\tilde{\mu}\,(-)$ is the microscopic, grain boundary friction coefficient, $\tilde{\sigma}_A$ is the normal stress acting on the inclined A-type grain boundaries and S_0 is the grain boundary cohesion.

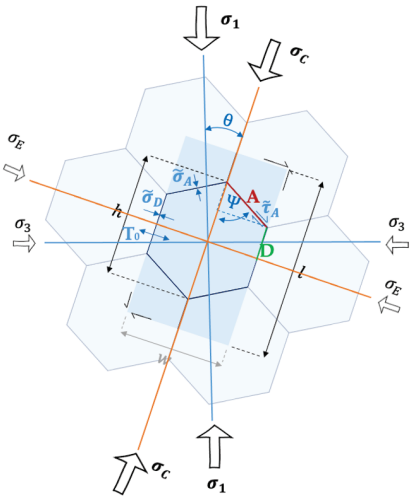

Figure 2: Microstructural model of hexagonal grain used to construct the GBFS-model, the unit cell is shown in shaded blue. The grain shape is defined by the apical angle (ψ) and aspect ratio ($R = \frac{h}{w}$) and its orientation with respect to the largest principal stress is denoted by θ. The grain boundaries along which sliding occurs (type A: $\tilde{\tau}_A = \tilde{\mu}\,\tilde{\sigma}_A + S_0$) and where tensile failure occurs (type D: $\tilde{\sigma}_D = -\tilde{T}_0$) are both indicated in the figure. σ_C, σ_E and are the normal stresses in the rotated axis frame.

Consider the shaded unit cell shown in Figure 2, and assume a compressive stress state$\sigma_1 > \sigma_2 = \sigma_3$ that is uniform for all unit cells and orientated at an angle θ with respect to the microstructure. This state leads to the following criterion for the dilatancy-boundary as defined by the GBFS model when θ is zero:

$$\sigma_1 - \sigma_3 = \left[\frac{(2R\tan(\psi)-1)(\tan(\psi)+\mu)}{\tan(\psi)(1-\mu(\tan(\psi))} - 1\right]\sigma_3 + \left[\frac{2T_0(R\tan(\psi)-1)(\tan(\psi)+\mu)+S_0(1+\tan^2\psi)}{\tan(\psi)(1-\mu(\tan(\psi))}\right] \quad (1)$$

in which $R = \frac{h}{w}$.

This dilatancy boundary can be represented by a linear function given by: $\sigma_1 - \sigma_3 = \Lambda\sigma_3 + B_0$, in which Λ is the slope of the dilatancy boundary and B_0 is its intercept. Alternatively, it can be represented by a linear relation between deviatoric stress and means stress, which can be directly compared with the empirical data shown in Figure 1 represented by $\sigma_{eq} = 1.56\bar{\sigma} + 3.47$, or obtained for natural salt and synthetic salt by previous authors (Peach 1991, Peach & Spiers 1996; Popp & Kern 2001 & Alkan et al. 2007).

To investigate whether the GBFS model can indeed describe the empirically derived dilatancy boundary, it is assumed that the tensile strength and the cohesion are both negligible. Realistic grain shapes are expected to have an aspect ratio (R) of 1-1.25 and the minimum friction coefficient $(\tilde{\mu})$ at salt grain boundaries, based on friction experiments by Bos et al. 2000 and Niemeijer & Spiers 2007 is 0.5. Minimizing the length of type D grain boundaries makes it more favorable for microcracking to occur, however it is expected that a grain of which the type D grain boundary $< \frac{w}{4}$ (face D $< \frac{w}{8}$) is unrealistic, as triple junctions of $\sim 120°$ are expected from microstructures. Model predictions for this range of parameter values and for $\theta = 0°$are shown in Figure 3a.

Tilting the grain with respect to the principal stress axes, such that 0 < θ < 30°, facilitates slip on inclined grain boundaries (type A) (see Figure 2). At the same time, tensile failure of type D grain boundaries becomes more difficult. For this range in θ, the GBFS criterion (for $S_0, T_0 = 0$) takes the form:

$$\sigma_1 - \sigma_3 = \left[\frac{(2A-2)}{(1+\cos(2\theta)-A+A\cos(2\theta)-B\sin(2\theta)}\right]\sigma_3 \quad (2)$$

In which $A = \frac{(2R\tan(\psi)-1)(\tan(\psi)+\mu)}{\tan(\psi)(1-\mu(\tan(\psi))}$ and $B = \frac{(2R\tan(\psi)-1)(1-\mu(\tan(\psi))-\tan(\psi)(\tan(\psi)+\mu)}{\tan(\psi)(1-\mu(\tan(\psi))}$.

When $\theta = 13°$, the slope of the dilatancy boundary is minimal ($\Lambda = 10.0$). This theoretical dilatancy boundary is plotted for $\psi = 60°, \mu = 0.5, R = 1.155$ in equivalent stress $(\sigma_1 - \sigma_3)$ vs. mean stress $((\sigma_1 + 2\sigma_3)/3)$ space in Figure 3a, alongside the predictions for the same shape where $\theta = 0°$. The empirical criterion shown in Figure 1a, which fits the dilatancy data obtained in our experiments, is added for comparison. Only predictions for unrealistic grain shapes (D $= \frac{w}{16}$, $\psi = 41.6°$, orange hexagon) approach the measured dilatancy boundary; reasonable values for R (≤ 1.25), ψ ($\geq 50°$) and μ (≥ 0.5), at all values of θ predict dilatancy at significantly higher differential stresses than observed experimentally. It can be concluded that the present GBFS-model for solid-solid grain boundary contacts (e.g. assuming dry grain boundaries or grain boundaries where any fluids present do not become over-pressured or wet the grain boundary) cannot account for dilatancy in rock salt.

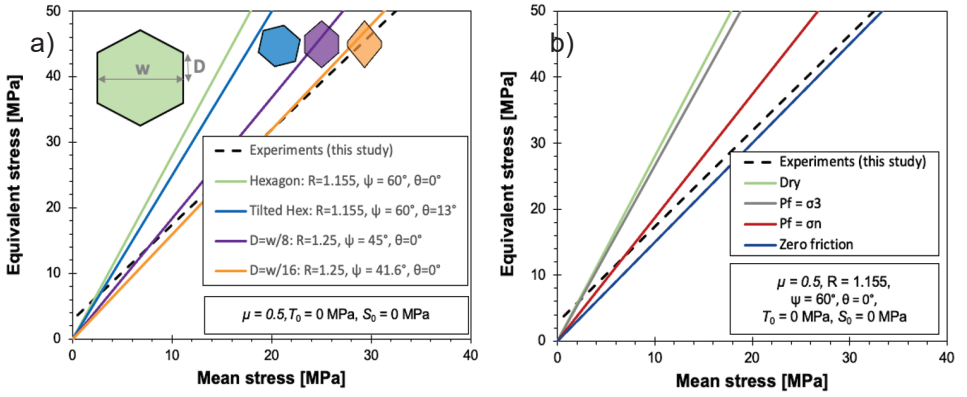

Figure 3: Dilatancy boundaries predicted by the GBFS-model compared to the dilatancy boundary derived from experiments in this study (equivalent stress vs. mean stress), for: (a) dry full solid-solid grain boundary contacts and (b) for grain boundaries containing inclusions taking up a fraction of 0.5 of the grain boundary, with a fluid pressure at respectively σ_3 and σ_n (the local normal stress on face A and D), and considering zero friction due to fluid lubrication. Note that the condition $P_f = \sigma_n$ (red line in b) represents the dilatancy boundary just before the inclusion becomes unstable as it represents the limit fluid pressure above which hydrofracture occurs. Also note that zero friction (blue line in b) does not imply that the intrinsic friction coefficient of the rock salt drops to zero, but that the effective normal stress is zero as the grain boundary is lubricated.

Let us now consider the possible effects of brine present in grain boundaries. There is widespread evidence for the presence of brine inclusions, channels and films in grain boundaries in natural rock salt (e.g. Urai et al. 1986), which may potentially affect grain boundary shear and tensile strength. Experiments on dry versus brine-saturated granular salt have shown that any chemical effect of brine on intergranular friction coefficient is close to negligible (Niemeijer & Spiers 2006). However, when inclusions are present at a pressure larger than 0, the grain boundary contact area decrease and the intrinsic grain boundary stress increases, which does affect the stress required to get dilatancy following the GBFS-model. Based on microstructural evidence (e.g. Urai et al. 1986), here it is assumed that inclusions take up 50% of the grain boundary contact area.

For brine-bearing grain boundaries, two end-member assumptions can be made regarding the brine pressure in inclusion arrays, channels or films: (1) the fluid pressure is equal to σ_3, which is a reasonable approximation for dilated salt near a fluid-filled borehole, assuming that the minimum principal stress (σ_3) normal to the borehole wall is equal to the fluid pressure; and (2) the fluid pressure in individual grain boundaries is equal to the local normal stress on the grain boundary (At face A: $P_f = \tilde{\sigma}_A$, At face D: $P_f = \tilde{\sigma}_D$). which both lower the dilatancy boundary (see Figure 3b). The case where the fluid pressure in the inclusions is equal to the local normal stress on the grain boundary must be considered as an upper limit as the inclusions cannot be stable at higher fluid pressures.

However, when the fluid in grain boundary inclusions or channels does increase beyond this stress the inclusions become over-pressured by compression of the grain boundary structure, reducing the effective normal stress and even “hydrofracturing” solid-solid contact points, then grain boundary frictional strength will be significantly further reduced compared with a dry grain boundary. Similarly, if thin, connected brine films form in grain boundaries due to dissolution of solid-solid contact points, hence spreading of fluid inclusions and associated dynamic wetting of the grain boundaries (see Van Oosterhout et al., this volume), then the effective

normal stress and frictional strength again fall to zero – provided the fluid film is not squeezed out from asperity contacts.

When the fluid inclusions become mobilized, the effective stress on the grain boundary is zero, and the dilatancy boundary (for $S_0, T_0 = 0$) is given by:

$$\sigma_1 - \sigma_3 = [2R\tan(\psi) - 2]\sigma_3 \quad (3)$$

For $\psi = 60°$ and $R = 1.155$, in the absence of an effective stress on the inclined grain boundary (face A), the slope of the dilatancy boundary (Λ) is 2.0 (see Figure 3b). This is very close to the slope of the dilatancy boundary observed in the dilatancy experiments in this study and previous work (e.g. Peach 1991; Peach & Spiers 1996; Popp & Kern 2001 & Alkan et al. 2007). Taking $\psi = 50°$ and $R = 1.25$ (at $\theta = 0°$, which is the most favorable orientated if the grain boundaries are lubricated) in combination with a lubricated grain boundary reduces the slope of the dilatancy boundary even further to $\Lambda = 1.6$.It can be concluded that the current GBFS model is able to explain the observed dilatancy boundary only when the grain boundaries are wetted and there is no grain boundary friction. Therefore, if the GBFS model applies, the dilatancy boundary obtained in our experiments and described in previous work should reflect a dilatancy boundary for “wet” rock salt with wetted grain boundaries. Based on this result, there should be a significant difference in the deviatoric stress required to obtain dilatancy in dried rock salt ($\Lambda > 10.0$) compared with wet rock salt ($\Lambda = 2.0$). However, no such effect is seen in our experimental results (see Figure 1b). The absence of any significant difference in dilatancy development in our dried and wet (undried and brine pressurized) Leinesteinsalz samples accordingly eliminates the possibility that dilatancy is controlled by intergranular slip on wet or dry grain boundaries (see Figure 1b).

4.2 Plastic strain incompatibility model

An alternative approach is that dilatancy in rock salt is caused by the plastic anisotropy of individual grains. While the crystal orientations of halite grains in rock salt are generally uniformly distributed (Kern 1977), favorably orientated grains deform more than unfavorably orientated grains. This indicates that the condition of complete strain compatibility between grains is not satisfied (Wenk et al. 1989) and Taylor’s classical model, that requires all crystals to deform at the same rate and therefore to undergo the same shape change as the polycrystal, does not apply for halite. For a polycrystalline aggregate to deform homogeneously, at least five independent slip-systems have to be active to satisfy the Von Mises condition for uniform strain in a polycrystalline aggregate (Von Mises 1928). Carter & Heard (1970) show that in halite at low temperatures, only the $\{110\} < 1\bar{1}0 >$ slip systems are active, meaning that the Von Mises conditions will not be satisfied, and that deformation and stress state will be heterogeneous from grain to grain with voids opening at grain boundaries when pressures are too low to force significant lattice bending or activation of additional slip systems.

Therefore, we have derived an exploratory model which assumes that dilatancy is caused by intergranular void opening related to plastic strain incompatibility (PSI). The PSI model is based on a simplified/idealized microstructure consisting of identical cubic grains of edge size d, subjected to principal stresses $\sigma_1, \sigma_2, \sigma_3$ applied perpendicular to the faces of the cube (see Figure 4). Here axi-symmetric conditions are considered ($\sigma_1 > \sigma_2 = \sigma_3$). The faces, e.g. the grain boundaries normal to the principal stresses, are assumed to have spaced fluid inclusions in island-channel form, of which the islands have an initial thickness ($w^0_{1,2,3}$) and island fraction area ($\alpha^0_{1,2,3}$) under atmospheric conditions (see Figure 4). From the grain boundary microstructure of natural salts, such as the Leinesteinsalz, we take the initial contact area fraction to be around 0.5, while the grain boundary (island-channel) thickness is assumed to be in the range of 0.5-5 µm (based on microstructural observations, e.g. Desbois et al. 2012), the grain size is taken to be 5 mm and the bulk modulus of salt is taken as 30 GPa (Warren, 2016).

It is assumed that individual grains and the grain boundary islands (contact points) deform both elastically and plastically and have the same elastic and plastic properties as the macroscopic aggregate determined from the work-hardening curve obtained in the present study under (near) non-dilatant, room temperature conditions (e.g. at 20 MPa). We describe the stress strain curve obtained at these conditions by $\varepsilon = f_m(\sigma) = A\sigma^n$, with $A = 5.7 \cdot 10^{-7}$ and $n = 3.1$, which gives an accurate fit. It is furthermore assumed that the plastic misfit strain increment (a volumetric strain) is proportional to the plastic axial strain according to the relation $d\varepsilon_v{}^+ = \beta d\varepsilon_1{}^{pl}$, in which β represents the misfit factor, which is estimated to be around $0.05 - 0.1$, to account for 2% positive volumetric strain under dilatant conditions at low confinement (2.5 MPa). After applying a confining pressure, axial loading (σ_a) is assumed to cause opening of triangular-sectioned grain boundary voids or cracks, with fixed aspect ratio ($a = \frac{h^+}{\Delta w^+}$), as a result of plastic misfit strain. The cracks are assumed to open on boundaries normal to σ_3 . At the same time, axial loading causes deformation of the islands present in grain boundaries normal to σ_1. The inclusions are assumed to be filled with brine at a pore pressure of 0. The compressive deformation of the islands (process 1) and the crack opening/growth (process 2) are indicated in Figure 4b. At present, any effect of crack closure by plastic intrusion into the opening crack (process 4) is not included in the model.

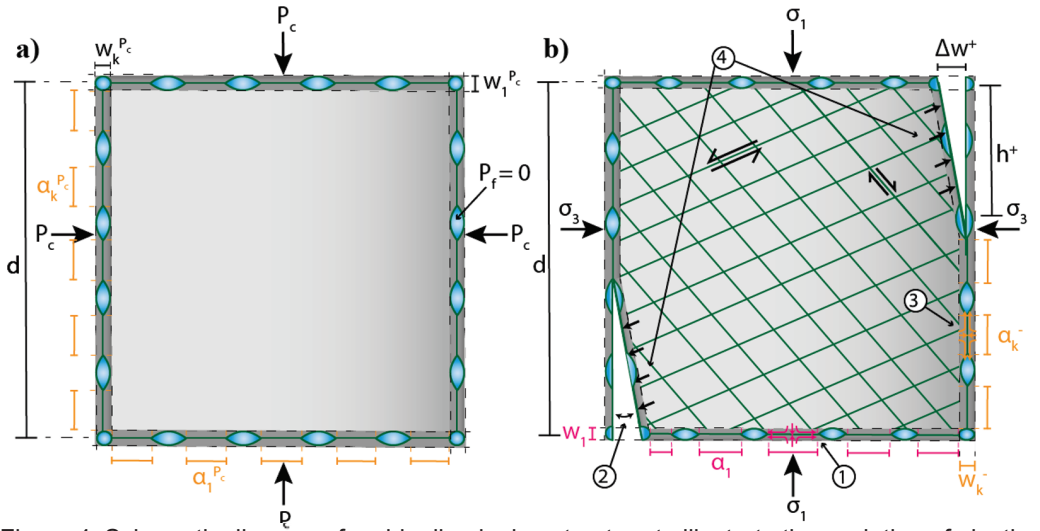

Figure 4: Schematic diagram of an idealized microstructure to illustrate the evolution of plastic strain incompatibility in rock salt under (a) hydrostatic conditions ($\sigma_1 = \sigma_3 = P_c$) and (b) under axial loading conditions$\sigma_1 > \sigma_3 = P_c$.

The stress-strain response as a result of axial loading at differential stress σ_a can now be written as:

$$\varepsilon_a = f_m(\sigma_a) - \left[f_m\left(\frac{\sigma_a + P_c}{\alpha_1}\right) - f_m\left(\frac{P_c}{\alpha_1{}^{Pc}}\right)\right]\frac{w^{Pc}}{d} \tag{4}$$

in which $\alpha_1{}^{Pc}$ and α_1 are respectively the strained contact area fractions of the horizontal grain boundaries after applying a confining pressure and axial loading, and w^{Pc} is the width of the grain boundaries after applying a confining pressure. The volumetric strain resulting from axial loading (compaction defined as positive) at differential stress σ_a is subsequently given by the relation:

$$\varepsilon_{va} = \frac{\sigma_a}{3K} + \left[f_m\left(\frac{\sigma_a + P_c}{\alpha_1}\right) - f_m\left(\frac{P_c}{\alpha_1{}^{Pc}}\right)\right]\frac{w^{Pc}}{d} - \beta[f_m(\sigma_a)] + \frac{w^{Pc}}{d}\left[f_m\left(\frac{P_c}{\alpha_k^-}\right) - f_m\left(\frac{P_c}{\alpha_k{}^{Pc}}\right)\right] \tag{5}$$

Here, the first term on the right hand side represent the elastic volumetric compression due to axial loading, the second term the volumetric compression of the grain boundaries normal to σ_1, the third term is the volumetric dilatation due to plastic misfit strains and the fourth term represents the volumetric compression of the grain boundaries normal to σ_3(which is equal to P_c), in which ${\alpha_k}^{P_c}$ is the contact area fraction of the vertical grain boundaries after applying a confining pressure and ${\alpha_k}^{-}$ is the contact area fraction of the vertical grain boundaries after dilatant crack opening, corrected for the length of the crack, which in turn is given by:

$$h^{+} = d\sqrt{\frac{a\beta[f_m(\sigma_a)]}{2}} \tag{6}$$

where a is the crack aspect ratio, here taken as 4 on the basis of microstructural observations. The volumetric strain evolution predicted by this set of equations (plus the assumption that all plastic flow occurs at constant volume) for a range of confining pressures is shown in Figure 5. The PSI-model successfully predicts the initial compaction and then dilatant behavior seen in at low confining pressure. However, the transition to non-dilatant behavior observed in experiments at high confining pressure, is not predicted by this model. This is presumably because plastic intrusion into opening cracks is not yet included. Further work on this is underway.

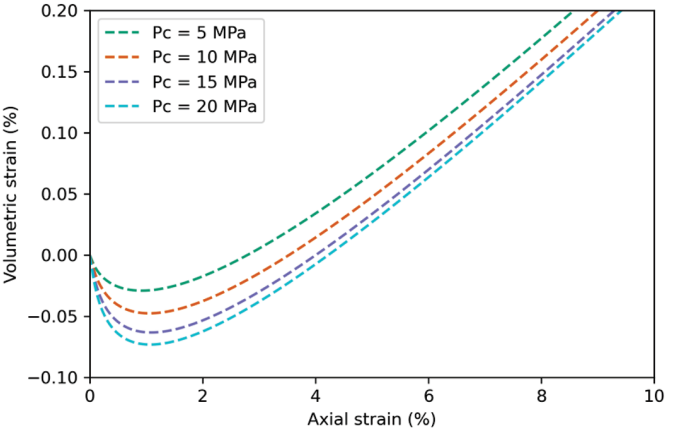

Figure 5: Volumetric strain evolution as a function of axial strain predicted by the PSI model for $\mathrm{P_c} = 5 - 20$ MPa.

5 Implications of experimental results on dilatancy in rock salt

The present experimental results confirm earlier work that dilatancy is limited to rock salt subjected to confining pressures at or below $15.0\ MPa$ or mean stresses $< 20.0\ MPa$. Based on the experimental results in this study, a linear dilatancy boundary has been constructed (see Figure 1a). Although, the dilatancy boundary can be extended to higher mean stresses, the strength of the samples measured at different strains, indicates that the differential stresses required to get dilatancy above a mean stress of $20.0\ MPa$ are not supported. Hence, the part of the dilatancy boundary that has a significant meaning is limited to a mean stress of $< 20\ MPa$. Based on the microphysical models described in this study, it can be excluded that frictional sliding in combination with tensile opening (e.g. the GBFS-model) is the sole mechanism governing dilatancy in rock salt. For any realistic grain shape, for full solid-solid contacts dilatancy by the means of frictional sliding will occur at much higher stresses than observed in experiments on dried samples. The PSI-model on the other hand does describe the observed behavior at low confining pressures ($\leq 10\ MPa$). However, it fails to describe a transition to non-dilatant behavior at higher confining pressures ($> 15\ MPa$). Further work on

the PSI-model is required to test whether plastic misfit strains, possibly in combination with local grain boundary slip, can account for the observed microstructural changes associated with dilatancy. At stresses near and certainly above the dilatancy boundary, it is expected that creep processes are accelerated due to the damage and the presence of a connected microcrack network (Alkan et al. 2009). Hampel 2012, describes a composite dilatancy model (CDM) to account for the reduction in load-baring capacity with increasing damage and dilatancy. In addition, they consider the effect of the access of humidity on enhancing creep rates once microcracks are present (see Hampel & Schulze 2017). However, both the influence of damage (δ_{dam}) and humidity (Θ) are modeled by empirical functions, based on an empirical dilatancy boundary given by $\sigma_{eq} = -0.0369 \cdot \bar{\sigma}^2 + 1.9663 \cdot \bar{\sigma} + 1.3001$. The CDM model allows for both the effect of a damage and humidity parameter to be $0 * f(\Theta, \delta_{dam})$ in the non-dilated field and rapidly rises to $1 * f(\Theta, \delta_{dam})$ near and above the dilatancy boundary. In this study, the aim is to derive a microphysical basis for the transition to dilatant behavior, which then can be used to account for the microstructural changes associated with dilatancy and directly related to estimate the acceleration of creep in the dilatant field. As such, the CDM model does not provide a microphysical basis for dilatancy either. The dilatancy boundary used for the CDM-model deviates to lower differential stresses around a mean effective stress of $15.0\ MPa$, with respect to the dilatancy boundary obtained from experiments in this study. Hence at mean effective stresses above $15.0\ MPa$, it is expected that the creep acceleration due to dilatancy based on our dilatancy boundary is modest compared to the CDM model. Although, a quantitative comparison is difficult as the CDM model and its parameters are entwined with the dilatancy boundary of their study.

6 Conclusions

Deformation experiments have been performed to investigate the influence of plastic deformation processes on dilatancy and permeability on natural Leinesteinsalz rock salt. The experiments were carried out in the work hardening flow regime at room temperature at strain rates of $4.8 \cdot 10^{-5}\ s^{-1}$. Two microphysical models were constructed in an attempt to explain the mechanisms causing dilatancy and microcrack development at the grain-scale, based on intergranular slip and plastic strain incompatibility. The principal results and conclusions are summarized below.

- Dilatancy in Leinesteinsalz is observed at confining pressures $\leq 15\ MPa$. No transition from non-dilated to dilated behavior is observed in experiments $> 15\ MPa$ and the stress/strain conditions at which dilatancy is expected to occur cannot be reached under conditions relevant for both natural and induced behavior.
- The experiments on Leinesteinsalz indicate that the dilatancy boundary can be described as a linear function of equivalent stress versus mean stress. This linear boundary has no meaning above a mean effective stress of $20\ MPa$, as the differential stress required for dilatancy is not supported by the sample.
- The GBFS-model cannot explain the observed dilatancy boundary unless grain boundary frictional resistance is zero. This condition can theoretically be achieved if mechanical loading results in coating of the grain boundaries with fluid films. However, the absence of any significant difference between dilatancy in dry and wet Leinesteinsalz eliminates the possibility that dilatancy in rock salt is controlled by intergranular frictional slip and the GBFS-model does not describe the mechanisms associated with dilatancy in rock salt.
- Dilatancy in rock salt is likely to be controlled by the opening of voids related to plastic misfit strains, which are compensated for by closure of voids by plastic compaction at higher confining pressures. Work is in progress to understand and model this better.

Acknowledgements

This study was part of the TKI-2017-08-UG-Rocksalt project. This project was carried out with a subsidy from the Dutch Ministry of Economic Affairs and Climate, National Schemes EZK-subsidies, Top Sector Energy and executed by Rijksdienst voor Ondernemend Nederland. We thank the consortium partners Shell Global Solutions, Nobian and TNO for their contribution, and the reviewers Judith Chester and Martyn Drury for their comments on the manuscript.

References

Alkan, H., Cinar, Y. & Pusch, G. 2007. Rock salt dilatancy boundary from combined acoustic emission and triaxial compression tests. International journal of rock mechanics and mining sciences, 44(1), 108-119.

Alkan, H. 2009. Percolation model for dilatancy-induced permeability of the excavation damaged zone in rock salt. *Int. J. Rock Mech. Min. Sci. 46 (4)*, pp. 716–724.

Bérest, P. & Brouard, B. 2003. Safety of salt caverns used for underground storage blow out; mechanical instability; seepage; cavern abandonment. *Oil & Gas Science and Technology*, 58.3: 361-384.

Bos, B., Peach, C.J. & Spiers, C.J. 2000. Slip behavior of simulated gouge-bearing faults under conditions favoring pressure solution. J. Geophys. Res. Solid Earth 105 (B7), pp. 16699–16717.

Carter, N.L. & Heard, H.C. 1970. Temperature and rate dependent deformation of halite. *Am. J. Sci.*

Celia, M.A., Bachu, S., Nordbotten, J.M., Kavetski, D. & Gasda, S.E. 2005. Modeling critical leakage pathways in a risk assessment framework: representation of abandoned wells. In: *Fourth Annual Conference on Carbon Capture and Sequestration DOE/NETL*.

Davies, R.J., Almond, S., Ward, R.S. Jackson, R.B., Adams, C., Worrall, F. Herringshaw, L.G., Gluyas, J.G. & Whitehead, M.A. 2015. Reply: “Oil and gas wells and their integrity: Implications for shale and unconventional resource exploitation”. *Mar. Pet. Geol. 59*, pp. 674–675.

Desbois, G., Urai, J.L., De Bresser, J.H.P. 2012. Fluid distribution in grain boundaries of natural fine-grained rock salt deformed at low differential stress (Qom Kuh salt fountain, central Iran): Implications for rheology and transport properties. *Journal of Structural Geology*, 2012, 43: 128-143.

Hampel, A. 2012. The CDM constitutive model for the mechanical behavior of rock salt: Recent developments and extensions. *Mechanical Behavior of Salt VII*, pp. 45-55.

Hampel, A. & Schulze, O. 2017. The composite dilatancy model: a constitutive model for the mechanical behavior of rock salt. *Mechanical behavior of salt-understanding of THMC processes in salt. CRC Press*, pp. 99-107.

Hunsche, U. 1998. Determination of dilatancy boundary and damage up to failure for four types of rock salt at different stress geometries. *Ser. rock soil Mech.*

Kern, H. 1977. Preferred orientation of experimentally deformed limestone marble, quartzite and rock salt at different temperatures and states of stress. *Tectonophysics 39 (1–3)*, pp. 103–120.

Khaledi, K., Mahmoudi, E., Datcheva, M. & Schanz, T. 2015. Stability and serviceability of underground energy storage caverns in rock salt subjected to mechanical cyclic loading. *Int. J. Rock Mech. Min. Sci. 86 (July)*, pp. 115–131.

Niemeijer, A.R. & Spiers, C.J. 2006. Velocity dependence of strength and healing behavior in simulated phyllosilicate-bearing fault gouge. *Tectonophysics 427 (1–4)*, pp. 231–253.

NIEMEIJER, A.R. & SPIERS, C.J. 2007. A microphysical model for strong velocity weakening in phyllosilicate-bearing fault gouges. *J. Geophys. Res. Solid Earth 112 (10)*, pp. 1–12.

ORLIC, B. & BUIJZE, L. 2014. Numerical modeling of wellbore closure by the creep of rock salt caprocks. In 48th US Rock Mechanics/Geomechanics Symposium. OnePetro.

PEACH, C.J., SPIERS, C.J., TRIMBY, P.W. 2001. Effect of confining pressure on dilatation, recrystallization, and flow of rock salt at 150 C. Journal of Geophysical Research: Solid Earth 160(B7), 13315-13328.

PEACH, C.J. 1991. Influence of deformation on the fluid transport properties of salt rocks (Doctoral dissertation, Faculteit Aardwetenschappen der Rijksuniversiteit te Utrecht).

POPP, T., KERN, H., & SCHULZE, O. 2001. Evolution of dilatancy and permeability in rock salt during hydrostatic compaction and triaxial deformation. Journal of geophysical research: Solid Earth, 106(B3), 4061-4078.

SUTHERLAND, H.J. & CAVE, S.P. 1980. Argon gas permeability of new mexico rock salt under hydrostatic compression. *Int. J. Rock Mech. Min. Sci. Geomech. 17 (5)*, pp. 281–288.

TRIMMER, D. 1982. Laboratory measurements of ultralow permeability of geologic materials. Rev. Sci. Instrum. 53 (8), pp. 1246–1254.

TSANG, C.F., BERNIER, F. & DAVIES, C. 2005. Geohydromechanical processes in the excavation damaged zone in crystalline rock, rock salt, and indurated and plastic clays – in the context of radioactive waste disposal. International Journal of Rock Mechanics and Mining Sciences, 42(1), 109–125.

VON MISES, R. 1928. Mechanik der plastischen Formänderung von Kristallen. *Zeitschrift für Angew. Math. und Mech.* pp. 161–185.

WARREN, J.K. 2016. Evaporites: A geological compendium. Springer.

WENK, H.R., CANOVA, G., MOLINARI, A. & MECKING, H. 1989. Texture development in halite: comparison of Taylor model and self-consistent theory. *Acta metallurgica*, 1989, 37.7: 2017-2029.